J Therm Anal Calorim
DOI 10.1007/s10973-015-4669-y

Synthesis and characterization of $Bi_{1-x}Nd_xFeO_3$ ($0 \leq x \leq 0.3$) prepared by thermal decomposition of $Bi_{1-x}Nd_x[Fe(CN)_6]\cdot 4H_2O$

M. C. Navarro[1] · G. Jorge[2] · R. M. Negri[3] · L. M. Saleh Medina[3] · M. I. Gómez[1]

Received: 26 November 2014 / Accepted: 22 March 2015

Abstract The series of polycrystalline heteronuclear complexes, $Bi_{1-x}Nd_x[Fe(CN)_6]\cdot 4H_2O$ ($0 \leq x \leq 0.3$), was successfully synthesized and characterized, by means of powder X-ray diffraction (PXRD) and infrared spectroscopy. The thermal behaviour was studied by thermogravimetric and differential thermal analysis. The crystal structure of the complexes was refined by Rietveld analysis. It was found that they crystallized in the orthorhombic crystal system, space group *Cmcm*. The lattice parameters and unit cell volume decrease with an increase in Nd concentration. In order to obtain the oxides $Bi_{1-x}Nd_xFeO_3$, the thermal decomposition of the inorganic complexes, $Bi_{1-x}Nd_x[Fe(CN)_6]\cdot 4H_2O$, has been investigated. By Rietveld analysis of PXRD data, the synthesis of the oxides was confirmed, evidencing in the series, a gradual change in crystal structure from rhombohedra to triclinic. Furthermore, with an increase in Nd content in $Bi_{1-x}Nd_xFeO_3$ oxides, impurity phases, such as Bi_2O_3, $Bi_2Fe_4O_9$ and $Bi_{25}FeO_{39}$ associated with the synthesis of $BiFeO_3$, are reduced. The morphology and chemical composition were investigated by microscopy electronic scattering and energy-dispersive X-ray spectroscopy. The electrical and magnetic properties have been determined to characterize the obtained oxides.

Keywords Hexacyanoferrate (III) · Rietveld method · X-ray diffraction · Thermal decomposition · Mixed oxides

Introduction

$BiFeO_3$ (BFO) is an important multiferroic material that has a rhombohedrally distorted perovskite structure with space group *R*3*c* [1, 2]. Two types of long-range ordering, G-type collinear antiferromagnetic ordering below 643 K and ferroelectric ordering below 1103 K coexist in BFO [3, 4]. Partial substitution of Bi by rare-earth ion, has attracted a lot of attention because it has proven to be a effective way to enhance and expand the applications of the BFO oxides [5–10]. Wu et al. [11] have synthesized by a sol–gel route $Bi_{1-x}Nd_xFeO_3$ powders of high purity, and they reported that a structural phase transition from the rhombohedral *R*3*c* to orthorhombic *Pnma* appears when the substituted Nd concentration is $0.125 \leq x \leq 0.15$N. Kumar et al. [12] synthesized the samples of $Bi_{1-x}Pr_xFeO_3$ ($0 \leq x \leq 0.15$) by conventional solid-state reaction method and observed that the magnetic Neel temperature (T_N) increases with increasing Pr content, and the antiferromagnetic (AFM) nature appears at 300 K. Chen et al. [13] have prepared $Bi_{1-x}La_xFeO_3$ (x = 0, 0.15, 0.30, 0.40) powders by the sol–gel–hydrothermal process, as a novel method to prepare mixed oxides.

In this preparation, $Bi_2Fe_4O_9$ is also obtained as a second phase [14], mainly due to the existence of Bi and Fe in

G. Jorge and R. M. Negri are members of the Research Career of CONICET.

✉ M. I. Gómez
mgomez@fbqf.unt.edu.ar

[1] Instituto de Química Inorgánica, Facultad de Bioquímica, Química y Farmacia, Universidad Nacional de Tucumán, Ayacucho 471, 4000 San Miguel de Tucumán, Argentina

[2] Instituto de Ciencias, Universidad Nacional de General Sarmiento, Buenos Aires, Argentina

[3] Instituto de Química Física de Materiales, Ambiente y Energía (INQUIMAE), Departamento de Química Inorgánica, Analítica y Química Física, Facultad de Ciencias Exactas y Naturales, Universidad de Buenos Aires, Buenos Aires, Argentina

Published online: 09 April 2015

BFO, and the generation and accumulation of oxygen vacancies [15].

Several methods have been reported to obtain $Bi_{1-x}Nd_xFeO_3$, and each has advantages and disadvantages [11, 13, 16]. The synthesis from the thermal decomposition of heteronuclear complexes has not been reported yet. The potentiality of this method to produce homogeneous powders with high surface area is due to the mixing of metal cations at the atomic level with the desired stoichiometry of the metals in the heteronuclear complex, allowing to obtain the oxides at lower temperatures than traditional methods [14, 17–24].

In the present work, we prepared and characterized the trimetallic heteronuclear complexes $Bi_{1-x}Nd_x[Fe(CN)_6]\cdot 4H_2O$ ($0 \leq x \leq 0.3$) as novel precursors to obtain mixed oxides ($Bi_{1-x}Nd_xFeO_3$) without the need for extreme conditions of temperature and pressure. We studied the thermal decomposition process by thermogravimetric and thermal differential analysis (TG–DTA), and the formation mechanism of a single phase of $Bi_{1-x}Nd_xFeO_3$ was also discussed. Mixed oxides obtained by this method have been well characterized by powder X-ray diffraction (PXRD), IR spectroscopy (IR) and scanning electron microscopy (SEM). A structural transition from rhombohedra to monoclinic phase was confirmed by PXRD and SEM. The electric properties and the variation in the magnetic behaviour of pure BFO Nd substituted are discussed.

Experimental

Synthesis of $Bi_{1-x}Nd_x[Fe(CN)_6]\cdot 4H_2O$ ($0 \leq x \leq 0.3$)

The trimetallic complexes $Bi_{1-x}Nd_x[Fe(CN)_6]\cdot 4H_2O$ were synthesized by mixing of aqueous solutions of $K_3[Fe(CN)_6]$, $Bi(NO_3)_3\cdot 5H_2O$ and $Nd(NO_3)_3\cdot 6H_2O$ in the adequate stoichiometric proportions, under stirring at room temperature. The obtained orange-red precipitate was filtered, thoroughly washed with water and ethanol, and finally, it stored in a dry box with silica gel.

Synthesis of $Bi_{1-x}Nd_xFeO_3$ ($0 \leq x \leq 0.3$)

The prepared complexes were grinded and then heated to 500 °C for 10 h in a furnace under air atmosphere in order to obtain powders of mixed oxides, $Bi_{1-x}Nd_xFeO_3$.

Characterization of $Bi_{1-x}Nd_x[Fe(CN)_6]\cdot 4H_2O$ and $Bi_{1-x}Nd_xFeO_3$ ($0 \leq x \leq 0.3$)

TG and DTA measurements for the complexes were carried out in Shimadzu TGA/DTA 50 equipments under flowing air (20 mL min^{-1}) at a heating rate of 5 °C min^{-1}, from room temperature to 770 °C. The measurements were made in platinum crucibles, and the amounts of sample were around 10 mg.

IR spectra (in the region of 4000–400 cm^{-1}) were recorded with a (FTIR) Perkin Elmer 1600 in transmission mode using KBr pellets. PXRD profiles were obtained in an X-Pert Pro PANalyticals diffractometer with Cu Kα radiation $\lambda = 1.5418$ Å.

The crystal structure refinements were performed by means of the Rietveld method [25] using FULLPROF program [26]. A pseudo-Voigt function convoluted with an axial divergence asymmetry function was chosen to generate the peak shapes. The following parameters were refined: zero point, scale factor, pseudo-Voigt parameters of the peak shape, atomic positions and cell parameters. $Bi[Fe(CN)_6]\cdot 4H_2O$ was used as initial model for the complexes [27] in the space group *Cmcm* and for the decomposition products, the model of $BiFeO_3$ in the space group *R*3*c* and *P*1 [16, 28].

Morphology and properties of $Bi_{1-x}Nd_xFeO_3$ ($0 \leq x \leq 0.3$)

The size and morphology of the particles were determined by SEM using a Zeiss Supra-55 VP microscope and a field emission scanning electron microscope (FESEM) Zeiss Supra 40 Gemini. Energy-dispersive X-ray spectroscopy (EDS) experiments were performed with an Oxford Instrument detector, model INCAx-Sight coupled to the Supra 40 Gemini device.

A Lake Shore 7400 vibrating sample magnetometer (VSM) was used for recording magnetization curves at room temperature. Powder samples were weighted (10–80 mg) and then packed with Teflon tape and mounted on the VSM sample holder. The magnetization curves were recorded from positive saturation at 1.8 T, in steps of 25 mT or less, with an integration constant of 10 s for each applied magnetic field.

Powders of $Bi_{1-x}Nd_xFeO_3$ were compressed at 100 kgf to form compressed disks (15 mm of diameter and thickness between 0.35 and 0.70 mm depending of each sample). The compressed disks were placed between two metallic electrodes in order to study its dc electrical properties. Polarization curves and leakage currents were measured with a Precision LC Materials Analyzer (Radiant Technologies). The polarization curves were recorded in a voltage range of [−99, +99 V]. The measurement begins at zero volts, followed by steps of 1 V until reaching +99 V, then proceeds to −99 V, and finally, it steps back to 0 V. The hysteresis period (duration of the entire hysteresis loop) was 12 ms, and a 1000 ms delay was applied before the measurement loop. Leakage currents were also measured in the range of [−99, +99 V], following a

similar procedure except for the voltage step that was 2 mV.

Results and discussion

Analysis of $Bi_{1-x}Nd_x[Fe(CN)_6]\cdot 4H_2O$ ($0 \leq x \leq 0.3$) complexes

IR spectroscopy

The results of IR spectra for the complexes are shown in Fig. 1. A broad ν(OH) hydrogen-bonded stretching band is observed in the range 3570–3000 cm^{-1}. Antisymmetric and symmetric ν(CN) stretching bands are observed in the range 2146–2117 cm^{-1} and $\delta(H_2O)$ bands in the range 1610–1630 cm^{-1}. The δ(M–C≡N) and ν(M–C) vibrations are observed at 595 and 430 cm^{-1}, respectively. These bands correspond to the expected frequency values for hexacyanometallates [17, 18].

Crystal structure refinement

Figure 2a shows the PXRD results for the $Bi_{1-x}Nd_x[Fe(CN)_6]\cdot 4H_2O$ ($0 \leq x \leq 0.3$) complexes. The PXRD peak positions are in agreement with that of $Bi[Fe(CN)_6]\cdot 4H_2O$ which has an orthorhombic unit cell (space group: *Cmcm*). Figure 2b plots the unit cell volume as a function of x. In all cases was observed that the volume decreases with an increase in x (Nd content), in agreement with the larger ionic radius of Bi^{3+} (1.17 Å) compared with that of Nd^{3+} (1.12 Å). In this orthorhombic structure, Fe^{3+} ions are coordinated to six C from cyano groups with the usual octahedral coordination (FeC_6), and Bi^{3+} and Nd^{3+} are 8-coordinated to six N atoms from cyano groups and two O from coordinated water molecules forming a bi-capped distorted trigonal prism (Bi, NdN_6O_2) as was reported in previous works [17, 29].

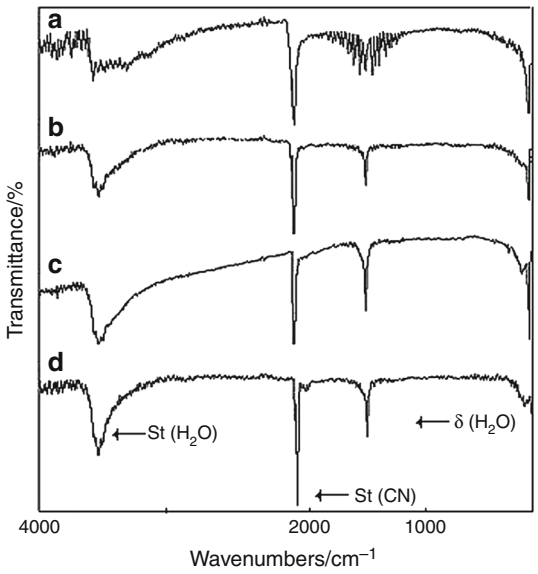

Fig. 1 IR spectra for the series of complexes $Bi_{1-x}Nd_x[Fe(CN)_6]\cdot 4H_2O$ ($0 \leq x \leq 0.3$). *a* $x = 0$; *b* $x = 0.1$; *c* $x = 0.2$; *d* $x = 0.3$

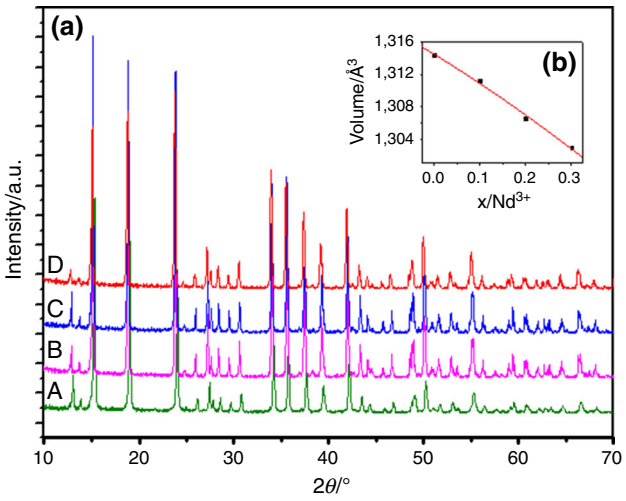

Fig. 2 *a* PXRD patterns for $Bi_{1-x}Nd_x[Fe(CN)_6]\cdot 4H_2O$ ($0 \leq x \leq 0.3$). *A* $x = 0$; *B* $x = 0.1$; *C* $x = 0.2$; *D* $x = 0.3$. *b Inset* Variation of cell volume with x

Table 1 shows the refined cell parameters and cell volume for $Bi_{1-x}Nd_x[Fe(CN)_6]\cdot 4H_2O$ ($0 \leq x \leq 0.3$) complexes.

Thermogravimetric analysis (TG) and differential thermal analysis (DTA) data

The thermal behaviour of the series $Bi_{1-x}Nd_x[Fe(CN)_6]\cdot 4H_2O$ ($0 \leq x \leq 0.3$) was studied by TG and DTA analysis. Figure 3 shows TG and DTA curves for the thermal decomposition of $Bi_{0.8}Nd_{0.2}[Fe(CN)_6]\cdot 4H_2O$. The TG curve indicates that the complex decomposes in four steps involving dehydration and decarboxylation. The first one ends at 140 °C with a mass loss of 11.60 % due to the elimination of three water molecules (theoretical value 11.25 %). The second one finishes at 165 °C with a mass loss of 3.78 % (theoretical value 3.75 %) and corresponds to the loss of the remaining water molecule to obtain the anhydrous complex. In DTA curve appear two endothermic peaks at 114 and 152 °C related to the two steps of dehydration.

The third step in TG, which finishes at 369 °C, has a mass loss of 20.36 % (theoretical value 21.35 %). This mass loss is attributed to the combustion of all the cyanide groups, but part of the CO_2 formed in this combustion clearly gets adsorbed on the surface of the particles as carbonate. This step turned out to be less steep than that of the undoped complex $Bi[Fe(CN)_6]$ ($x = 0$) [14] that means that complexes doped with Nd are decomposed more slowly [17].

Table 1 Crystallographic parameters for $Bi_{1-x}Nd_x[Fe(CN)_6]\cdot 4H_2O$ ($0 \leq x \leq 0.3$) after Rietveld refinement of XRPD data at room temperature

Compound	SG	*a*/Å	*b*/Å	*c*/Å	*V*/Å^3
$Bi[Fe(CN)_6]\cdot 4H_2O$	*Cmcm*	7.4527 (1)	12.8697 (1)	13.7037 (2)	1314.33
$Bi_{0.9}Nd_{0.1}[Fe(CN)_6]\cdot 4H_2O$	*Cmcm*	7.4498 (2)	12.8527 (1)	13.6941 (1)	1311.21
$Bi_{0.8}Nd_{0.2}[Fe(CN)_6]\cdot 4H_2O$	*Cmcm*	7.4431 (2)	12.8418 (1)	13.6706 (3)	1306.67
$Bi_{0.7}Nd_{0.3}[Fe(CN)_6]\cdot 4H_2O$	*Cmcm*	7.4364 (2)	12.8286 (2)	13.6571 (1)	1302.87

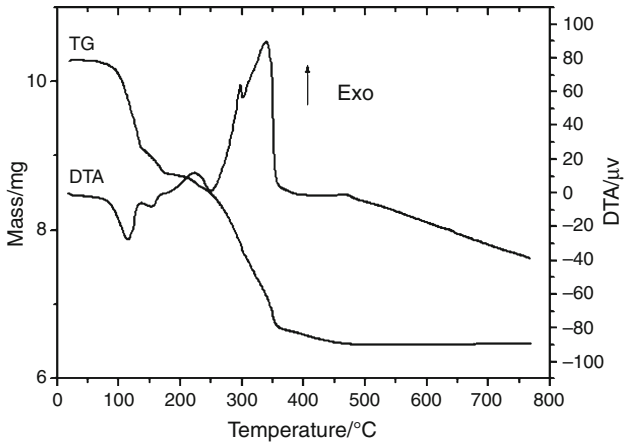

Fig. 3 TG and DTA curves for $Bi_{0.8}Nd_{0.2}[Fe(CN)_6]\cdot 4H_2O$

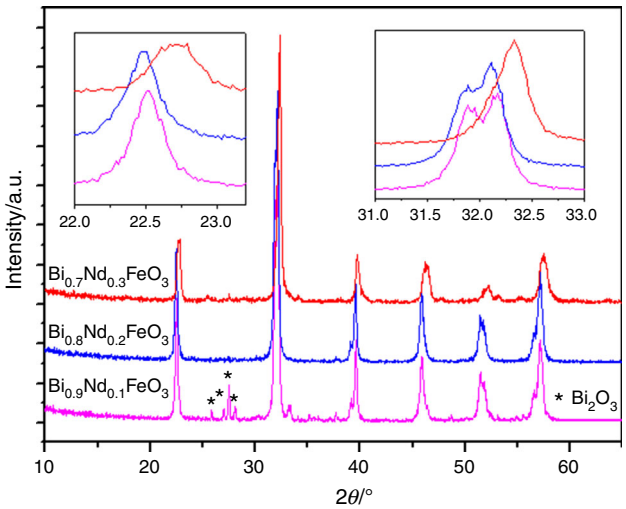

Fig. 4 PXRD patterns for $Bi_{1-x}Nd_xFeO_3$ (x = 0.1, 0.2, and 0.3)

The fourth step has a mass loss of 1.93 % (theoretical value 2.03 %) and corresponds to the simultaneous loss of the surface CO_3^{2-} and O_2 uptake to generate the mixed oxides. In the range from 230 to 490 °C, the DTA curve shows an endothermic peak and two intensive exothermic peaks.

The total mass loss from room temperature to 500 °C is 37.44 %, and it is in agreement with the theoretical mass loss 37.51 % for the formation of $Bi_{0.8}Nd_{0.2}FeO_3$ from the complex. The final product was confirmed by PXRD, FTIR spectroscopy and EDS.

It is observed that the decomposition process for substituted complex ends at a higher temperature than the corresponding Bi (x = 0), but at lower temperature than the corresponding complex of Nd (x = 1) [14, 17].

The decomposition mechanism of the doped complexes is similar to that of the previously reported pure bismuth complex [14], where the solid products of each step were identified by X-ray diffraction and IR spectroscopy.

The sequence of decomposition steps could be expressed as:

$$Bi_{0.8}Nd_{0.2}\left[Fe(CN)_6\right]\cdot 4H_2O_{(s)}\ \theta \rightarrow Bi_{0.8}Nd_{0.2}\left[Fe(CN)_6\right]\cdot H_2O_{(s)} + 3H_2O_{(g)} \quad (1)$$

$$Bi_{0.8}Nd_{0.2}\left[Fe(CN)_6\right]\cdot H_2O_{(s)}\ \theta \rightarrow Bi_{0.8}Nd_{0.2}\left[Fe(CN)_6\right]_{(s)} + H_2O_{(g)} \quad (2)$$

$$Bi_{0.8}Nd_{0.2}\left[Fe(CN)_6\right]_{(s)} + {}^{15}/_{8}\ O_{2(g)}\ \theta \rightarrow {}^{1}/_{4}\ Bi_{0.8}Nd_{0.2}FeO_{3(s)} + {}^{1}/_{20}\ Bi_2O_{3(s)} + {}^{3}/_{40}\ Nd_2O_{3(s)} + {}^{3}/_{8}\ Fe_2O_{3(s)} + {}^{1}/_{4}\ (BiO)_2CO_{3(s)} + {}^{1}/_{4}\ NO_{(g)} + {}^{23}/_{8}\ C_2N_{2(g)} \quad (3)$$

$${}^{1}/_{4}\ Bi_{0.8}Nd_{0.2}FeO_{3(s)} + {}^{1}/_{20}\ Bi_2O_{3(s)} + {}^{3}/_{40}\ Nd_2O_{3(s)} + {}^{3}/_{8}\ Fe_2O_{3(s)} + {}^{1}/_{4}\ (BiO)_2CO_{3(s)}\ \theta \rightarrow Bi_{0.8}Nd_{0.2}FeO_{3(s)} + {}^{1}/_{4}\ CO_{2(g)} \quad (4)$$

The complete reaction could be written as:

$$Bi_{0.8}Nd_{0.2}\left[Fe(CN)_6\right]\cdot 4H_2O_{(s)} + {}^{15}/_{8}\ O_{2(g)}\ \theta \rightarrow Bi_{0.8}Nd_{0.2}FeO_{3(s)} + 4H_2O_{(g)} + {}^{1}/_{4}\ NO_{(g)} + {}^{23}/_{8}\ C_2N_{2(g)} + {}^{1}/_{4}\ CO_{2(g)} \quad (5)$$

Analysis of $Bi_{1-x}Nd_xFeO_3$ oxides

Crystal structure refinement

Figure 4 shows the PXRD result for the residues of thermal decomposition at 500 °C for x = 0.1, 0.2 and 0.3. In the

Table 2 Crystallographic parameters and discrepancy factors for $Bi_{1-x}Nd_xFeO_3$ ($0 \leq x \leq 0.3$) after Rietveld refinement of XRPD data

Compound	SG	*a*/Å	*b*/Å	*c*/Å	*V*/Å^3	Discrepancy factors
$BiFeO_3$	*R*3c	5.5798 (5)	5.5798 (5)	13.8370 (2)	373.09	$R_{wp} = 15.7$ $R_{Bragg} = 3.90$
$Bi_{0.9}Nd_{0.1}FeO_3$	*R*3c	5.5771 (2)	5.5771 (2)	13.8399 (2)	372.79	$R_{wp} = 14.3$ $R_{Bragg} = 2.91$
$Bi_{0.8}Nd_{0.2}FeO_3$	*R*3c	5.5740 (2)	5.5740 (2)	13.8229 (3)	371.93	$R_{wp} = 14.8$ $R_{Bragg} = 2.73$
$Bi_{0.7}Nd_{0.3}FeO_3$	*P*1	3.8952 (1)	3.9157 (1)	3.9377 (1)	60.06	$R_{wp} = 16.2$ $R_{Bragg} = 3.41$

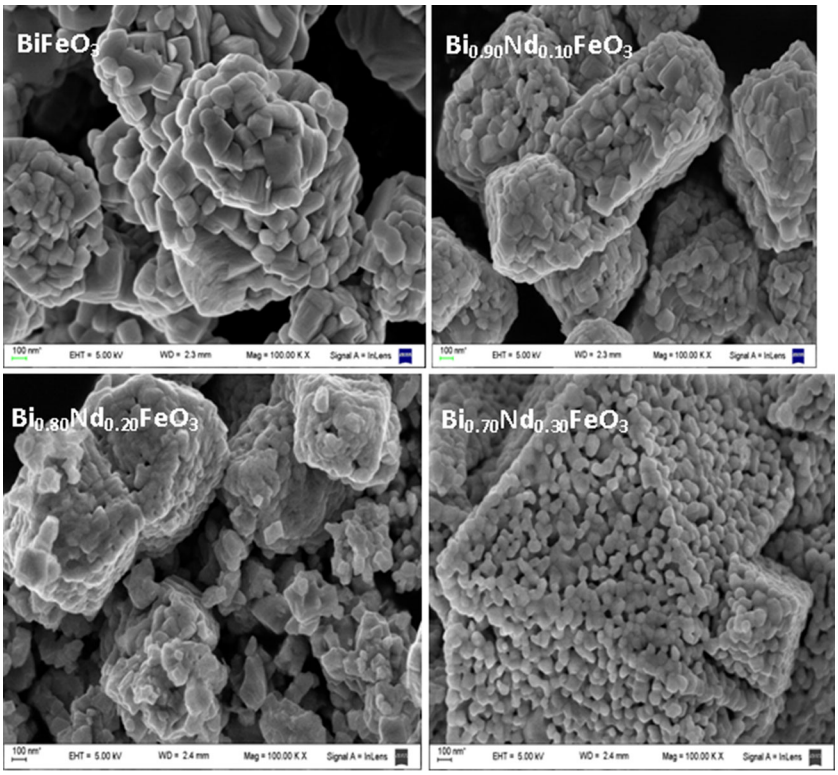

Fig. 5 SEM images of $Bi_{1-x}Nd_xFeO_3$ compounds (x = 0, 0.1, 0.2 and 0.3, as indicated; magnification ×100,000 in all cases)

case of $x = 0.1$, beside the peaks associated with single-phase $Bi_{0.9}Nd_{0.1}FeO_3$ type perovskite structure, it observed peaks corresponding to Bi_2O_3 phase. For $x = 0.2$, only the peaks associated with the single-phase type perovskite are observed. These samples show cell parameters very similar to those informed to $BiFeO_3$, which has a rhombohedra structure with *R*3*c* space group. For $x = 0.3$, we found that the oxide has a triclinic structure with *P*1 space group, as result of replacing in major proportion the large Bi^{3+} ions by the smaller Nd^{3+}. The calculated parameters after refinement are listed in Table 2. The change in cell parameters and decrease in volume indicate the successful substitution of Nd at Bi sites, following the Vegard's law for ideal solid solutions [30]. An expansion of the peaks position around 22.6 and 32 in 2θ is shown in inset of Fig. 4. These variations of the diffraction peaks related to structural phase transition are observed.

SEM images and EDS analysis

SEM images of Nd-doped samples are shown in Fig. 5. The observed grains form almost regular polygons, which are an indicative of their excellent degree of crystallinity, in agreement with the X-ray diffractograms shown in Fig. 4.

The SEM images show that $BiFeO_3$ and $Bi_{1-x}Nd_xFeO_3$ ($0.1 \leq x \leq 0.2$) are prism-like particles, while for $x = 0.3$ is more sphere-like. In both cases, they are highly agglomerated, just like those previously reported for yttrium-doped bismuth ferrites obtained by acid–base co-precipitation [31]. The size of the particles is shown in Table 3. It can be seen that the addition of Nd produces a decreasing in the size of the particles for $x = 0.3$. The representative energy-dispersive spectra of the $Bi_{1-x}Nd_xFeO_3$ nanoparticles confirmed the presence of Bi, Nd, Fe and O. Table 3 shows the average

Table 3 Size of the particles and average percentage values of each element in the $Bi_{1-x}Nd_xFeO_3$ oxides ($0 \leq x \leq 0.3$)

Sample	Size[a] (a ≈ b)	Size[b] (h)	Bi[c]	Bi[d]	Nd[c]	Nd[d]	Fe[c]	Fe[d]	O[c]	O[d]
$BiFeO_3$	212 ± 43	113 ± 20	20	18	0	0	20	19	63	60
$Bi_{0.90}Nd_{0.10}FeO_3$	58 ± 12	112 ± 22	18	19	2	1	20	28	52	60
$Bi_{0.80}Nd_{0.20}FeO_3$	75 ± 18	143 ± 34	16	18	4	1	20	18	63	60
$Bi_{0.70}Nd_{0.30}FeO_3$		72 ± 30*	14	15	6	4	20	22	59	60

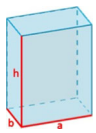

[a] Depth and height of the prism shown on the inset, in nm

[b] Length of the depth and height of the prism shown on the inset, in nm; *radius of the spherical-like particle

[c] Expected atomic percentage from stoichiometry, considering only one pure phase is formed

[d] Measured atomic percentage determined by EDS

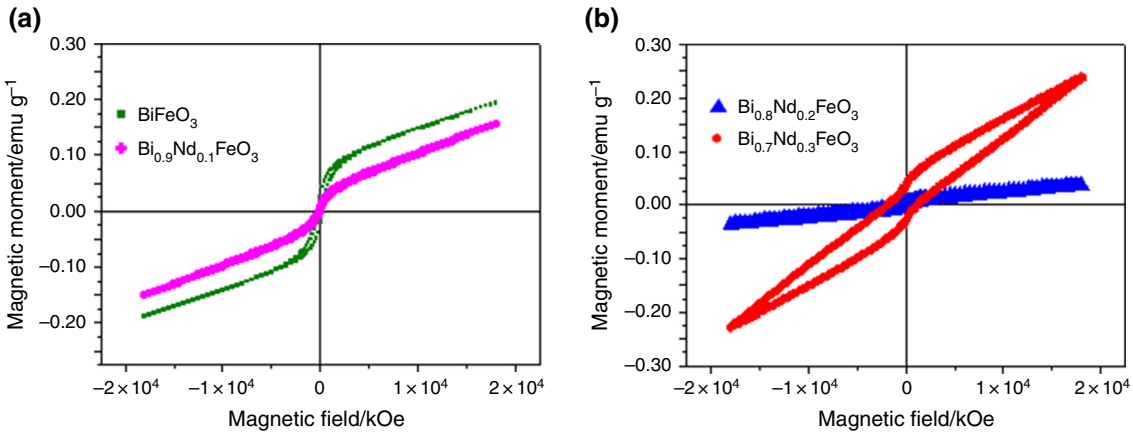

Fig. 6 Magnetization curves at room temperature of $Bi_{1-x}Nd_xFeO_3$ non-compressed powders. **a** $x = 0$, 0.1; **b** $x = 0.2$ and 0.3

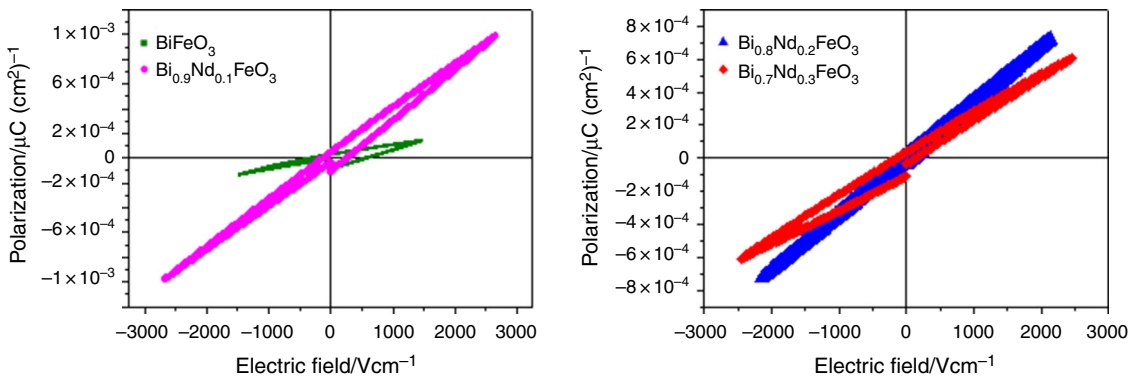

Fig. 7 Electric polarization curves of $Bi_{1-x}Nd_xFeO_3$ compressed disks at room temperature ($x = 0$, 0.1, 0.2 and 0.3). Variation of polarization (surface density charge) with applied electric field

percentage values of each element in the samples. The detected amounts are smaller than stoichiometric amounts added during synthesis.

Magnetic and electric properties

Figure 6a, b shows the magnetization curves of $Bi_{1-x}Nd_xFeO_3$ non-compressed powders at room temperature. It seems that samples with $x = 0$ and 0.1 (Fig. 6a) present a super-paramagnetic behaviour at room temperature. Samples with $x = 0.2$ and 0.3 seem to have a different behaviour than those with $x = 0$ and 0.1. For instance, sample with $x = 0.2$ is likely paramagnetic, but sample with $x = 0.3$ appears in a ferromagnetic state (see Fig. 6b). Although these characteristics are not easy to explain, it is remarkable that the sample where structural changes was detected ($x = 0.3$) is the only one which presents a ferromagnetic behaviour (see Tables 2, 3).

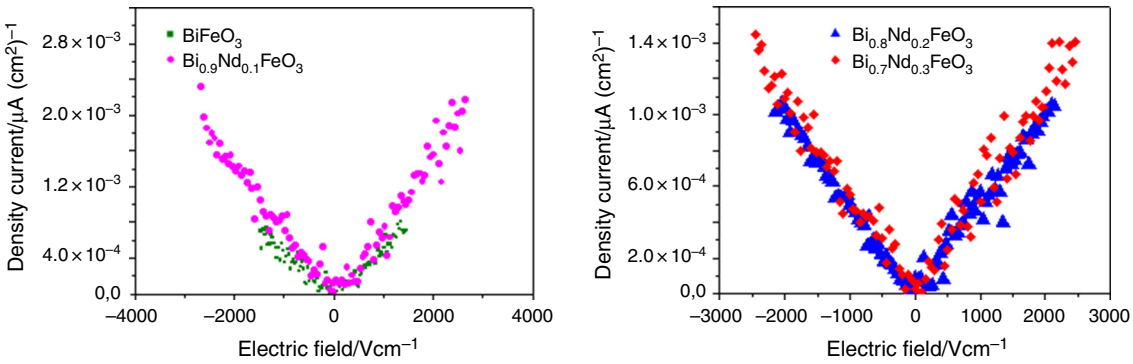

Fig. 8 Leakage currents of $Bi_{1-x}Nd_xFeO_3$ compressed disks at room temperature (x = 0, 0.1, 0.2 and 0.3). Variation of density current with applied electric field

The magnetic behaviour of $BiFeO_3$ is still a matter of theoretical discussion, since several magnetoelectric effects contribute and/or compensate the final magnetic properties which can be modified by doping [31–33].

Figure 7 shows the properties of compressed disks of $Bi_{1-x}Nd_xFeO_3$. In all cases, likely paraelectric behaviour was observed. The measured curves for Nd-doped compounds present larger polarization values when compared with the undoped compound ($BiFeO_3$). On the other hand, the measured values of polarization are relatively low, if they are compared with the reported values by Wang et al. [34]. These authors observed that non-sintered samples present lower values than those sintered and that the electrical polarization increases with sintering temperature. Additionally, it has been observed that another important factor is the used pressure to compress the samples. Large values of polarization are achieved by compressing the powders at tens of MPa [34, 35]. The pressure applied in this study is 0.57 MPa. Therefore, the low observed polarization (Fig. 7) can be related to the fact that samples were not sintered and the applied pressure to compress the powders was relatively low.

The leakage currents of $Bi_{1-x}Nd_xFeO_3$ compressed disks (Fig. 8) are very low compared to similar compounds (for instance when comparing with yttrium-doped bismuth ferrites [31]), which made them very useful to be used as capacitors or other electronic devices. We can observe that the addition of neodymium has not a relevant influence on the density of electric current.

Conclusions

We have successfully synthesized $Bi_{1-x}Nd_x[Fe(CN)_6]\cdot 4H_2O$ ($0 \leq x \leq 0.3$) complexes. All the complexes can be fitted in orthorhombic *Cmcm* space group. The volume cell was decreased with an increased Nd content, due to that the ionic radius of Nd^{3+} is smaller than the one of Bi^{3+}. Thermal decomposition of the complexes takes place in four stages. The first two correspond to the loss of water molecules; the third one correspond to the elimination of cyanide with formation of surface carbonates, and the last step corresponds to the simultaneous loss of the CO_3^{2-} and O_2 uptake to form mixed oxides.

By thermal decomposition of the complexes, at temperatures as low as 500 °C, we successfully obtained $Bi_{1-x}Nd_xFeO_3$ ($0 \leq x \leq 0.3$) mixed oxides with type perovskite structure, space group $R3c$ for x = 0, 0.1 and 0.2 and $P1$ for x = 0.3. Further with Nd substitution, impurity phases such as Bi_2O_3, $Bi_2Fe_4O_9$ and $Bi_{25}FeO_{39}$ are reduced, especially for the mixed oxide with x = 0.2.

SEM images show that oxides $BiFeO_3$ and $Bi_{1-x}Nd_xFeO_3$ ($0.1 \leq x \leq 0.2$) show prism-like particles, while $Bi_{0.7}Nd_{0.3}FeO_3$ is more sphere-like. Also, the addition of Nd reduces the size of the particles.

The $Bi_{1-x}Nd_xFeO_3$ oxides present superparaelectric behaviour, with larger polarization for the Nd-doped oxides compared to $BiFeO_3$. The magnetization curves appear also in the super-paramagnetic regime, with lower magnetization values for the Nd-doped compounds compared to $BiFeO_3$, except for sample doped with 30 % Nd. Leakage currents are lower than those reported for similar ceramics doped with rare earth.

Acknowledgements G. J. and R. M. N. thank CONICET, FONCYT for PICT 2011-0377 and PICT-2012-0717, and UBACyT for projects 2002 01101 00098 and 2002 201001 00142. L. M. S. M. thanks CONICET for fellowship. M. C. N. and M. I. G. thank CIUNT for financial support, Project 26D-428 and 26D-517. The authors thank Laboratorio de Bajas Temperaturas (UBA) for magnetic measurements and the Center of Advanced Microscopy (CMA-UBA) for SEM images.

References

1. Hill NA, Filippetti A. Why are there any magnetic ferroelectrics? J Magn Magn Mater. 2002;242(245):976–9.
2. Hur N, Park S, Sharma PA, Ahn JA, Guha S, Cheong SW. Electric polarization reversal and memory in a multiferroic material induced by magnetic fields. Nature. 2004;429:392–5.
3. Sosnowka I, Neumair TP. Spiral magnetic ordering in bismuth ferrite. J Phys C: Solid State Phys. 1982;15:4835–46.

4. Kaczmarek W, Pajak Z. Differential thermal analysis of phase transitions in $Bi_{1-x}La_xFeO_3$ solid solution solid. State Commun. 1975;17:807–10.
5. Khodabakhsh M, Sen C, Kassaf H, Gulgun MA, Misirlioglu IB. Strong smearing and disappearance of phase transitions into polar phases due to inhomogeneous lattice strains induced by A-site doping in $Bi_{1-x}A_xFeO_3$ (A: La, Sm, Gd). J Alloys Comp. 2014;604:117–29.
6. Pikula T, Dzik J, Lisinska-Czekaj A, Czekaj D, Jartych E. Structure and hyperfine interactions in $Bi_{1-x}Nd_xFeO_3$ solid solutions prepared by solid-state sintering. J Alloys Comp. 2014;606:1–6.
7. Luo L, Wei W, Yuan X, Shen K, Xu M, Xu Q. Multiferroic properties of Y-doped $BiFeO_3$. J Alloys Comp. 2012;540:36–8.
8. James Vineetha, Prabhakar Rao P, Sameera S, Divya S. Multiferroic based reddish brown pigments: $Bi_{1-x}M_xFeO_3$ (M=Y and La) for coloring applications. Ceram Int. 2014;40:2229–35.
9. Sharma P, Varshney D, Satapathy S, Gupta PK. Effect of Pr substitution on structural and electrical properties of $BiFeO_3$ ceramics. Mater Chem Phys. 2014;143–2:629–36.
10. Dutta PD, Mandal BP, Naik R, Lawes G, Tyagi AK. Magnetic, ferroelectric, and magnetocapacitive properties of sonochemically synthesized Sc-doped $BiFeO_3$ nanoparticles. J Phys Chem. 2013;117:2382–9.
11. Wu YJ, Chen XK, Zang J, Chen XJ. Magnetic enhancement across a ferroelectric-antiferroelectric phase boundary in $Bi_{1-x}Nd_xFeO_3$. J Appl Phys. 2012;111:053927–32.
12. Kumar N, Panwar N, Gahtori B, Singh N, Kishan H, Awana VPS. Structural dielectric and magnetic properties of Pr substituted $Bi_{1-x}PrxFeO3$ ($0 \leq x \leq 0.15$). J Alloys Comp. 2010;501:129–32.
13. Chen Z, Hu J, Lu Z, He X. Low-temperature preparation of lanthanum-doped $BiFeO_3$ crystallites by a sol-gel-hydrothermal method. Ceram Int. 2011;37:2359–64.
14. Navarro MC, Lagarrigue MC, De Paoli JM, Carbonio RE, Gómez MI. A new method of synthesis of $BiFeO_3$ prepared by thermal decomposition of $Bi[Fe(CN)_6]\cdot 4H_2O$. J Therm Anal Calorim. 2010;102:655–60.
15. Chen DG, Tang XG, Liu QX, Cheng XF, Zou Y. The Nd-doping effect on dielectric abnormity of $BiFeO_3$ ceramics below the Néel temperature. Mater Sci Forum. 2011;687:439–46.
16. Kumar A, Varshney D. Crystal structure refinement of $Bi_{1-x}Nd_xFeO_3$ multiferroic by the Rietveld method. Ceram Int. 2012;38:3935–42.
17. Navarro MC, Pannunzio-Miner EV, Pagola S, Gómez MI, Carbonio RE. Structural refinement of $Nd[Fe(CN)_6]\cdot 4H_2O$ and study of $NdFeO_3$ obtained by its oxidative thermal decomposition at very low temperatures. J Solid State Chem. 2005;178:847–54.
18. Gil DM, Navarro MC, Lagarrigue MC, Guimpel J, Carbonio RE, Gómez MI. Crystal structure refinement, spectroscopic study and magnetic properties of yttrium hexacyanoferrate(III). J Mol Struct. 2011;1003:129–33.
19. Gil DM, Navarro MC, Lagarrigue MC, Guimpel J, Carbonio RE, Gómez MI. Synthesis and structural characterization of perovskite $YFeO_3$ by thermal decomposition of a cyano complex precursor, $Y[Fe(CN)_6]\cdot 4H_2O$. J Therm Anal Calorim. 2011;103:889–96.
20. Gil DM, Guimpel J, Paesano A, Carbonio RE, Gómez MI. $Y[Fe_{1-x}Cox(CN)6]\cdot 4H2O$ ($0 \leq x \leq 1$) solid solutions: synthesis, crystal structure, thermal decomposition and spectroscopic and magnetic properties. J Mol Struct. 2012;1015:112–7.
21. Seto Y, Umemoto K, Arii T, Masuda Y. Synthesis and thermal decomposition of lanthanide hexacyanochromate(iii) complexes, $Ln[Cr(CN)_6]\cdot nH_2O$ (Ln = La-Lu; $n = 3, 4$). J Therm Anal Calorim. 2004;76:166–77.
22. Sawano R, Masuda Y. Studies on synthesis and magnetic property of $Ln_xEu_{1-x}CoO_3$ (Ln = Gd, Ho; $x = 0 \sim 1$) prepared by means of thermal decomposition of $Ln_xEu_{1-x}[Co(CN)_6]\cdot nH_2O$ (Ln = Gd, Ho; $x = 0 \sim 1$). J Therm Anal Calorim. 2008;92:413–8.
23. Medina Córdoba L, Echeverria G, Piro O, Gómez MI. Ammonium, barium hexacyanoferrate(II) trihydrate: synthesis, crystal structure, thermal decomposition and spectroscopic study. J Therm Anal Calorim. 2015;. doi:10.1007/s10973-015-4492-5.
24. Kumar Swamy N, Pavan Kumar N, Venugopal Reddy P, Gupta M, Shanmukharao Samatham S, Venkateshwarulu D, Ganesan V, Malik V, Das BK. Specific heat and magnetocaloric effect studies in multiferroic $YMnO_3$. J Therm Anal Calorim. 2014;. doi:10.1007/s10973-014-4223-3.
25. Young RA. The Rietveld method. Oxford: Oxford Scientifics Publications; 1995.
26. Rodriguez-Carvajal J. Recent advances in magnetic structure determination by neutron powder diffraction. Phys B. 1993;192:55–69.
27. Mullica DF, Perkins HO, Sappenfield EL. Synthesis, spectroscopic studies, and crystal and molecular structure of bismuth hexacyanoferrate(III) tetrahydrate, $Bi[Fe(CN)_6]\cdot 4H_2O$. Inorg Chim Acta. 1988;142:9–12.
28. Sosnowska I, Schaefer W, Kockelmann W, Andeersen KH, Toyanchuk IO. Crystal structure and spiral magnetic ordering of BiFeO3 doped with manganese. Appl Phys A. 2002;74:1040–2.
29. Gil DM, Carbonio RE, Gómez MI. Crystal structure refinement and vibrational analysis of $Y[Co(CN)6]\cdot 4H2O$ and its thermal decomposition products. J Mol Struct. 2013;1041:23–8.
30. West AR. Solid state chemistry and its applications. New York: Wiley; 1994.
31. Saleh Medina LM, Guillermo AJ, Negri RM. Structural, dielectric and magnetic properties of $Bi_{1-x}Y_xFeO_3$ ($0 \leq x \leq 0.2$) obtained by acid–base co-precipitation. J Alloys Comp. 2014;592:306–12.
32. Kadomtseva AM, Popov YF, Pytakov AP, Vorob'ev GP, Zvezdin AK, Viehlands D. Phase transitions in multiferroic $BiFeO_3$ crystals, thin-layers, and ceramics: enduring potential for a single phase, room-temperature magnetoelectric 'holy grail. Phase Transit. 2006;79:1019–42.
33. Park TJ, Papaefthymiou GC, Viescas AJ, Moodenbaugh AR, Wong SS. Sie-dependent magnetic properties of single-crystalline multiferroic $BiFeO_3$ nanoparticles. Nano Lett. 2007;7:766–72.
34. Wang YP, Zhou L, Zhang MF, Chen XY, Liu JM, Liu ZG. Room-temperature saturated ferroelectric polarization in $BiFeO_3$ ceramics synthesized by rapid liquid phase sintering. Appl Phys Lett. 2004;84:1731–3.
35. Yu B, Li M, Guo D, Pei L, Zhao X. Effects of ion doping at different sites on electrical properties of multiferroic $BiFeO_3$ ceramics. J Phys D Appl Phys. 2008;41:065003.